Advances in Engineering Software 198 (2024) 103789

Contents lists available at ScienceDirect

Advances in Engineering Software

journal homepage: www.elsevier.com/locate/advengsoft

# Form finding of cable-membrane structures with flexible frames: Finite element implementation and application to surface accuracy analysis of umbrella-like rib-mesh reflectors

Shiran Zhu [a], Ruiwen Guo [b], Xin Jin [c], Xiaofei Ma [c], Jinxiong Zhou [b], Ning An [a,*]

[a] Key Laboratory of Advanced Spatial Mechanism and Intelligent Spacecraft, Ministry of Education, School of Aeronautics and Astronautics, Sichuan University, Chengdu 610065, People's Republic of China

[b] State Key Laboratory for Strength and Vibration of Mechanical Structures and School of Aerospace, Xi'an Jiaotong University, Xi'an 710049, People's Republic of China

[c] Xi'an Institute of Space Radio Technology, Xi'an 710100, People's Republic of China

ARTICLE INFO

*Keywords:*
Form finding
Finite element method
Umbrella-like antenna
Rib-mesh reflector
Cable-membrane structure

ABSTRACT

Deployable rib-mesh reflector antennas, known for their ultralight nature and high deployment-to-stowage ratio, have been attracting attention from both the aerospace industry and academia. Form finding is a critical step in determining the equilibrium shape of the reflector under a specific internal stress distribution, which is a prerequisite in evaluating the surface accuracy of these antennas. This paper presents a comprehensive methodology for iteratively implementing the nonlinear finite element method for form finding of cable-membrane structures supported by flexible frames. The method is integrated into the commercial finite element code ABAQUS with Python scripts, and its accuracy and efficiency are validated through a few benchmark examples. Subsequently, the proposed method is applied to analyze the surface accuracy of umbrella-like rib-mesh reflector antennas. The effect of key design parameters such as the number and rigidity of ribs, the magnitude and anisotropy of membrane stress, and the amount of pretension force in boundary cables on the antenna's surface accuracy has been highlighted. The effort not only establishes a robust and user-friendly strategy for form finding of cable-membrane structures supported by flexible frames but also provides valuable insights into the surface accuracy of umbrella-like rib-mesh reflector antennas. To facilitate the application of the FEM-based form-finding method, the source code for this paper is publicly available via a permanent link on GitHub https://github.com/SCU-An-Group/FEM-based-Form-Finding.

## 1. Introduction

Tensile cable-membrane structures, typically supported by frames, provide innovative designs to create lightweight, aesthetically pleasing, and functional structures. Their versatile applications extend across daily life and diverse industries, ranging from common items like umbrellas and tents to complex industrial structures such as large-span membrane roofs and spaceborne deployable reflector antennas [1–5]. Among them, deployable mesh reflectors play an important role in the design of large-scale satellite deployable antennas, due to their ultralight nature, ease of folding and deployment, high deployment-to-stowage ratio, and facilitation of large diameter realization [4]. Fig. 1(a) shows a schematic diagram of a deployable mesh reflector antenna that has an umbrella-like shape at the on-orbit working state. As shown in Fig. 1(b), this type of umbrella antenna consists mainly of a central hub, a series of parabolic radial ribs, and a reflective metallic mesh surface with boundary cables. The metallic mesh surface and boundary cables serve as tensile structures, characterized by negligible flexural stiffness and limited to undergoing tension stress to maintain structural integrity [6,7]. The parabolic radial ribs serve as supporting frames to preserve the overall rigidity and stability of the antenna.

According to the rigidity of antenna ribs, the umbrella antenna can be categorized into two families: rigid-rib antennas and flexible-rib antennas, each employing different folding and deployment mechanisms. The deployment of the rigid-rib antenna is typically actuated using electric motors located at the base, in conjunction with torsion springs positioned at the hinges of antenna ribs. Examples of rigid-rib antennas include the Ka-band Radar Parabolic Deployable Antenna (KaRPDA) proposed by NASA and JPL for the Radar in a CubeSat (RainCube) mission [8], and the X-band Synthetic Aperture Radar (SAR) antenna

* Corresponding author.
*E-mail address:* anning@scu.edu.cn (N. An).

https://doi.org/10.1016/j.advengsoft.2024.103789
Received 23 August 2024; Accepted 1 October 2024
Available online 8 October 2024

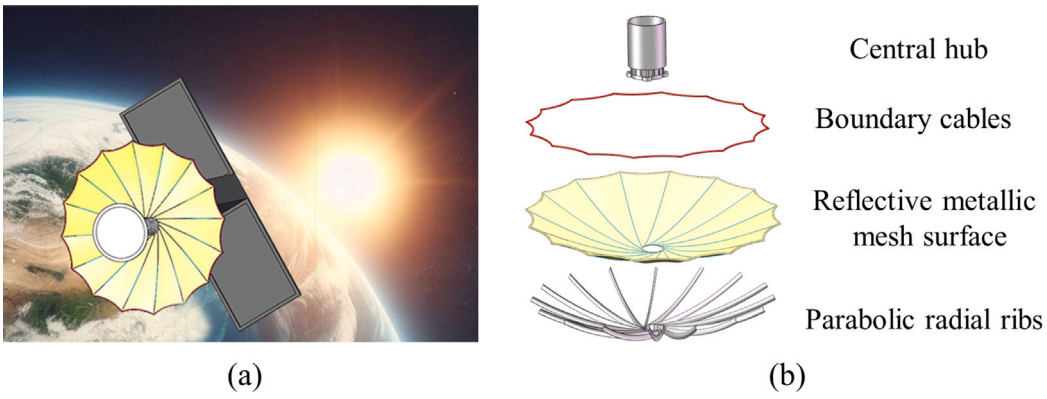


**Fig. 1.** Schematic diagram of (a) the working state of the umbrella-like space deployable rib-mesh reflector antenna, and (b) its constitutive parts: a central hub, a number of parabolic radial ribs, a metallic mesh reflective surface, and boundary cables.

developed by Indian Space Research Organisation for the Radar Imaging Satellite (RISAT 2B/R1/R2). On the other hand, for the flexible-rib antenna, deployment is often actuated by the stored strain energy in the deformation of flexible ribs. A notable example of flexible-rib antennas is the wrapped-rib antenna, for which the flexible ribs, made of either metallic or fiber polymer composite materials, are stowed by being elastically wrapped around the central hub before launch, and once in orbit, the ribs are then released to deploy the mesh reflector into a working state [9,10]. Earlier, the US AST-6 satellite adopts this type of antenna, with a diameter of 9.1 meters [11]. Recently, researchers from the Oxford Space System Ltd in UK [12], Chiba University in Japan [13], and Tongji University in China [14], proposed a variety of wrapped-rib antenna prototypes with apertures of 2.7 m, 3.6 m, and 0.5 m, respectively. In addition to the wrapped-rib antenna, there are also other types of foldable and deployable flexible-rib antennas. Pellegrino et al. [15,16] proposed an antenna design featuring a 1.5-meter diameter Collapsible Rib-Tensioned Surface (CRTS) reflector, where flexible ribs were folded around the central hub, and a flat Kevlar-reinforced Kapton foil was utilized as the reflective surface. Shape memory alloys (SMA) are smart materials that are capable of returning to a predefined shape when subjected to electric heating. This unique property makes them highly suitable for the design of self-deployable structures [17]. Lim et al. [18] designed and fabricated a 2-meter diameter deployable parabolic antenna that utilizes SMA as flexible ribs and a fabric sheet membrane as the reflector.

From a mechanical perspective, the mesh reflector umbrella-like antenna can be recognized as a tensile structural system composed of cable-membrane structures supported by frames. In the deployed state, the mesh reflector establishes an equilibrium shape as a result of the balance between the imposed boundary conditions provided by the supporting frames and the predefined tensile stress within the reflector membrane and boundary cables. Discovering the optimal equilibrium form for the membrane reflector requires a rigorous form-finding process, for which numerous methods have been developed over the past several decades. A comprehensive review of these methods can be found in [19]. Among them, the force density method (FDM) and the finite element method (FEM) are most widely used in the form finding of large deployable mesh reflector antennas [20].

The FDM was initially proposed for cable networks by Schek [21] and subsequently enhanced by Maurin and Motro [22] to extend its applicability to membranes. In recent years, FDM has been extensively utilized and enhanced for the form finding of large deployable mesh reflector antennas [23]. Tang and Li [24] developed an equivalent-force density method by identifying the equivalent axial force density and equivalent transversal force density to replace the prestress in triangular and quadrilateral membrane elements. Gu et al. [25] proposed an approach to solve the equivalent problem of membrane stress based on the virtual work principle, by which they extended the surface density method to the form-finding of orthotopic membrane structures. Researchers have also realized that the flexible deformation of supporting frames has a significant influence on the nodal positions of the cable networks, necessitating the inclusion of frame deformation in the form finding procedure of cable networks. Yuan et al. [26] proposed a form finding method to address the elastic deformation of the supporting structures in large deployable mesh reflectors. Nie et al. [27] proposed a form finding and design optimization approach for cable network structures with flexible frames. The deformation of cable networks and supporting frames are coupled to model the equilibrium state in an optimization model. Liu et al. [28] combined the force density method with the nonlinear finite element method to account for the geometrical nonlinearity and flexible deformation of the deployable ribs in the form finding design procedure of cable networks.

Although the FDM has been well developed and widely employed in surface accuracy analysis for large deployable reflector antennas, most of the existing analyses have focused on the form finding of pretensioned cable networks for loop mesh reflector antennas, with the AstroMesh reflector antenna [29] serving as an example. The form finding and surface accuracy analysis of umbrella-like rib-mesh antennas have remained largely unexplored. For an umbrella-like antenna, the mesh reflector can be directly supported by the parabolic radial ribs, and the boundary cables are only utilized for maintaining the form of the membrane. The FEM offers an alternative approach for determining the equilibrium form of umbrella-like antenna reflector [14,30]. Nonlinear FEM is particularly effective in solving the nonlinear deformation of membranes, cables, and flexible frames under predefined stress states [31]. A significant challenge in using FEM for form-finding problems is that tensile structures often deform under uniform stress, resulting in an altered, non-uniform stress distribution. Consequently, achieving a uniformly distributed stress state in equilibrium typically requires multiple iterations to refine the geometry [32]. Optimization algorithms can used to facilitate these iterations, which however entails a substantial computational cost [20,27,33,34]. Bletziner et al. [35,36] proposed an updated reference strategy that addresses the form finding task by iteratively updating the reference configuration with the deformed configuration until the stresses in tensile structures converge uniformly. The idea has been widely integrated with nonlinear FEM and applied to solve form-finding problems of cable-membrane structures in both civil engineering [1,37,38] and aerospace engineering [14,39,40].

To efficiently address the form-finding of umbrella-like reflector antennas, this paper integrates the nonlinear FEM method with the commercial software ABAQUS, utilizing Python scripts to automate the iteration procedure. The fundamental mechanics principles and implementation details of the method are documented, followed by solving several benchmark cases to validate its accuracy and efficiency. Subsequently, the proposed method is employed to conduct form finding of umbrella-like mesh reflector antennas, focusing on evaluating the

effect of key structural design parameters on the surface accuracy of the antenna. The design parameters investigated in this paper include the number and rigidity of radial ribs, the magnitude and anisotropy of pretension stress in the membrane, and the amount of pretension force applied to the boundary cables.

The remaining parts of the paper are organized as follows. Section 2 provides an overview of the continuum mechanics description and finite element implementation details integral to the iteratively updated reference strategy for form-finding. Section 3 presents a series of numerical examples solved through the proposed method for verification and validation. In Section 4, the method is applied to conduct surface accuracy analyses of umbrella-like rib-mesh reflector antennas. Parametric studies are performed to study the effect of several key design parameters on the surface accuracy performance of the antenna. Finally, the paper concludes with Section 5, summarizing the key contribution and insights derived from the study.

## 2. Methodology

### 2.1. Fundamental mechanics

Tensile structures, such as cables and membranes, rely on tension stress to maintain their shape and structural integrity. These structures are typically tensioned and supported by frames to create a stable form. However, the equilibrium shape of tensile structures is not initially known and needs to be determined. Form finding is the method to determine the equilibrium shape of tensile structures concerning a specifically prescribed tension stress state and given boundary conditions. As the equilibrium shape is unknown, form finding involves an iterative process to refine the geometry of the structure until it reaches a state where all forces are in equilibrium and the structure satisfies the prescribed tension stress and boundary conditions. The iterative process begins with defining the desired tension stress distribution to an initial reference configuration. The initial reference configuration satisfies the boundary conditions and serves as a starting point for further iterations. The response of tensile structures is assumed based on the hypothesis of large displacements, large rotations, but small strains, and the material behavior can be modeled using the St. Venant–Kirchhoff material model [36]. Let $\mathbf{F} = \partial\mathbf{x}/\partial\mathbf{X}$ be the deformation gradient, mapping a material point from the reference position $\mathbf{X}$ to its current position $\mathbf{x}$, and $J$ be its determinant, $J = \det \mathbf{F}$. The strain energy density of the St. Venant–Kirchhoff material is given by

$$\psi(\mathbf{E}) = \frac{1}{2}\lambda(\mathrm{tr}(\mathbf{E}))^2 + \mu\mathrm{tr}(\mathbf{E}^2) \tag{1}$$

where $\mathbf{E} = \frac{1}{2}(\mathbf{F}^T\mathbf{F} - \mathbf{I})$ is the Green–Lagrange strain tensor. $\lambda$ and $\mu$ are the Lamé parameters, which are related to the material property through Young's modulus $E$ and Poisson ratio $\nu$ by $\lambda = \frac{E\nu}{(1+\nu)(1-2\nu)}$ and $\mu = \frac{E}{2(1+\nu)}$. The second Piola–Kirchhoff stress $\mathbf{S}$ is given by

$$\mathbf{S} = \frac{\partial\psi}{\partial\mathbf{E}} = \lambda\mathrm{tr}(\mathbf{E})\mathbf{I} + 2\mu\mathbf{E} \tag{2}$$

The Cauthy stress tensor is then obtained as

$$\boldsymbol{\sigma} = \frac{1}{J}\mathbf{F}\cdot\mathbf{S}\cdot\mathbf{F}^T \tag{3}$$

which establishes equilibrium at the current configuration in the absence of body forces by satisfying

$$\mathrm{Div}\ \boldsymbol{\sigma} = 0. \tag{4}$$

It should be noted that although the Cauthy stress $\boldsymbol{\sigma}$ achieves equilibrium at the current configuration, it usually results in a non-homogeneous distribution due to the deformation of the material. Recall that the fundamental objective of form finding is to identify an optimal configuration that achieves equilibrium while preserving the prescribed homogeneous internal stress. This intricate task necessitates iterative procedures to systematically update the configuration until the sought equilibrium configuration with the prescribed stress is attained. The basic idea of the iteratively updated reference strategy method is illustrated in Fig. 2. First, a homogeneous internal stress $\mathbf{S}$ is applied to the initial reference configuration $\Omega_0$. The material undergoes deformation, transitioning the reference configuration to the current configuration by solving the static equilibrium. Next, the current configuration is designated as a new reference configuration $\Omega_1$, on which the non-homogeneous Cauthy stress is removed, and the homogeneous stress state $\mathbf{S}$ is applied once again. This process iterates until the deformation converges to a sufficiently small value, i.e., the deformation gradient $\mathbf{F}$ approaches the identity matrix $\mathbf{I}$, and the calculated Cauthy stress $\boldsymbol{\sigma}$ approximates the prescribed homogeneous stress. The final configuration $\Omega_n$ represents the optimal equilibrium shape that achieves equilibrium with the prescribed homogeneous stress state.

### 2.2. Finite element implementation

The above-described form finding theory has been implemented in the commercial finite element code ABAQUS with the help of the scripting interface. This section provides details on the implementation of the method, including the modeling of cable, membrane, and frame elements, as well as the intricacies of the form finding strategy.

#### 2.2.1. Cable

The cable is modeled as a linear elastic material characterized by its elastic modulus $E$ and Poisson ratio $\nu$. It behaves like a rod when subjected to a tensile load but loses stiffness upon reaching compression. In ABAQUS, truss elements are employed to represent the cable, and the "no compression" material option is utilized to negate the material stiffness in compression. The pretension force in the cable is induced through the use of a virtual temperature change load $\Delta T$ in conjunction with a fictitious coefficient of thermal expansion (CTE) $\alpha$. The thermal strain $\epsilon^{\mathrm{therm}}$ in the cable along its longitudinal direction is given as

$$\epsilon^{\mathrm{therm}} = \alpha\Delta T. \tag{5}$$

Considering a scenario where the cable is constrained at both ends, see Fig. 3(a), the total strain $\epsilon$ in the cable is the sum of its mechanical strain $\epsilon^{mech}$ and thermal strain $\epsilon^{therm}$, and equals 0.

$$\epsilon = \epsilon^{mech} + \epsilon^{therm} = 0 \tag{6}$$

Using Hooke's law, the internal stress induced in the cable can be determined as

$$\sigma = E\epsilon^{mech} = -E\epsilon^{therm} \tag{7}$$

Combining Eqs. (5) and (7), and considering that the tension force $T = \sigma A$, we can express the tension force in the cable as

$$T = -EA\alpha\Delta T \tag{8}$$

where A is the cross-section area of the cable. Eq. (8) elucidates that the pretension force in the cable can be introduced by applying a virtual temperature load and an artificial CTE for the cable material. The negative sign implies that the tension force shall be introduced by inducing a decrease in temperature, supposing that a positive CTE is assumed.

#### 2.2.2. Membrane

The mesh reflector is modeled using membrane elements in ABAQUS, which offer stiffness only in the plane of the element without bending or transverse shear stiffness, i.e., the membrane is in a state of plane stress. The pretension stress is also introduced by using virtual temperature loads with the artificial CTE. As illustrated in Fig. 3(b), the membrane features two in-plane directions, allowing for prescribing distinct stress values along each direction. This flexibility can be achieved by assuming two different CTEs tailored to the respective

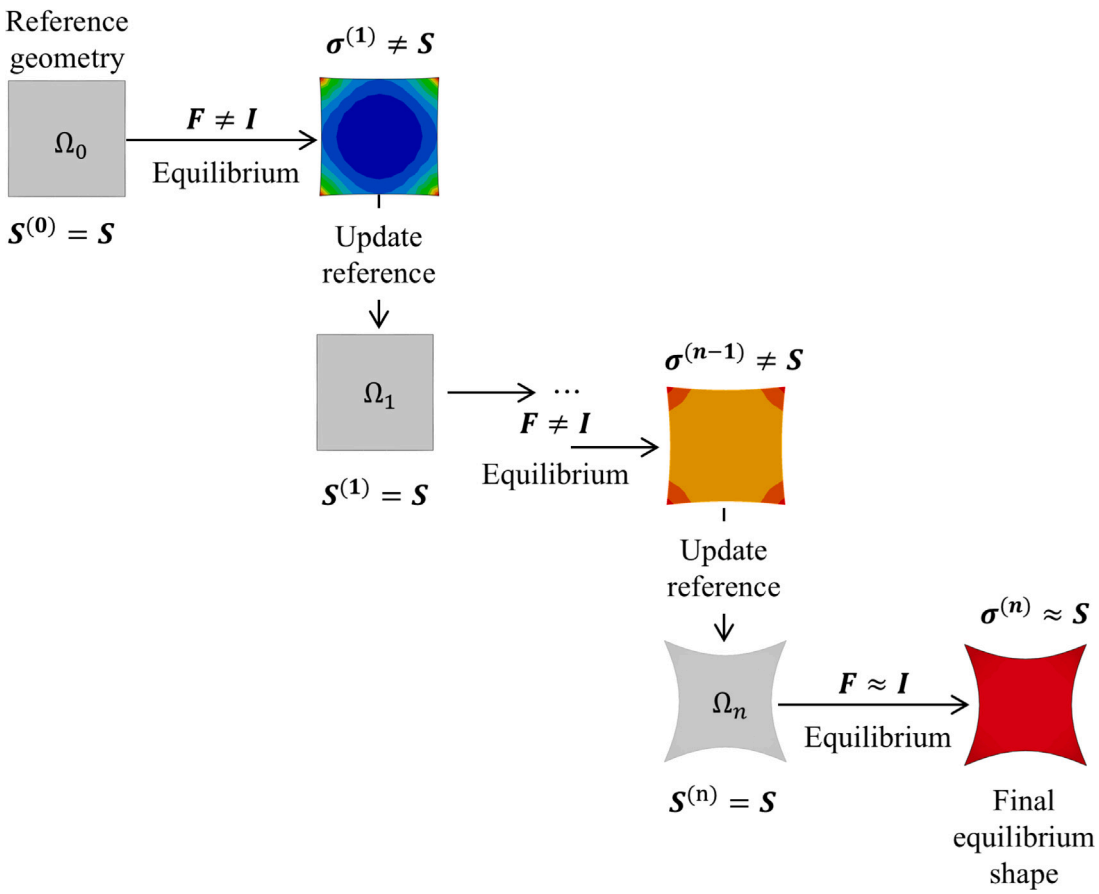


**Fig. 2.** Schematic of the nonlinear FEM method for form finding. The final optimal equilibrium shape of the tensile structure is obtained by iteratively updating the reference configuration with an FEM-calculated deformed configuration.

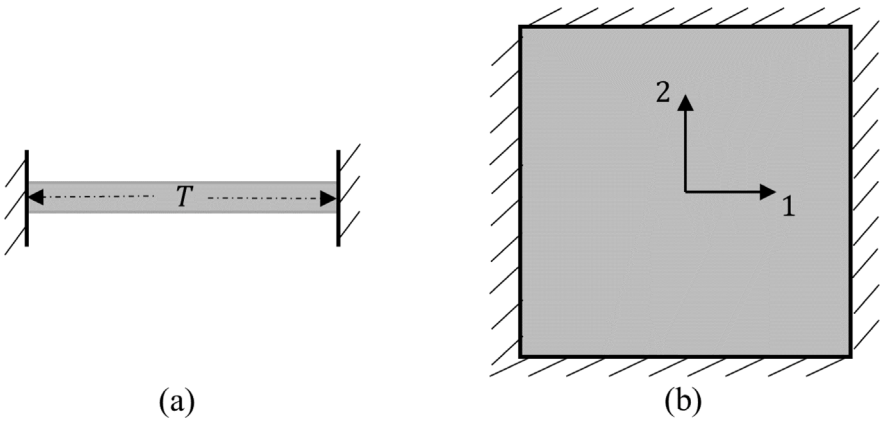


**Fig. 3.** Modeling pretension in the (a) cable and (b) membrane by applying virtual temperature loads and artificial CTEs of the tensile material.

directions. Herein, the CTEs along 1- and 2-directions are denoted as $\alpha_1$ and $\alpha_2$, respectively. When the membrane undergoes a temperature change of $\Delta T$, the resulting thermal strains in the two directions are given by

$$\varepsilon_1^{therm} = \alpha_1 \Delta T \quad \text{and} \quad \varepsilon_2^{therm} = \alpha_2 \Delta T. \tag{9}$$

Assuming the membrane is fully constrained at all boundary edges, resulting in zero total strains in both directions, the mechanical strains are expressed as

$$\varepsilon_1^{mech} = -\varepsilon_1^{therm} \quad \text{and} \quad \varepsilon_2^{mech} = -\varepsilon_2^{therm}. \tag{10}$$

Then, for a linear elastic material characterized by Young's modulus $E$ and Poisson's ratio $\nu$, the generalized Hooke's law relates the mechanical stress and strain for the plane stress state as follows

$$\sigma_1 = \frac{E}{1-\nu^2}\varepsilon_1^{mech} + \frac{\nu E}{1-\nu^2}\varepsilon_2^{mech}, \tag{11}$$

and

$$\sigma_2 = \frac{\nu E}{1-\nu^2}\varepsilon_1^{mech} + \frac{E}{1-\nu^2}\varepsilon_2^{mech}. \tag{12}$$

A combination of Eqs. (9)–(12) gives rise to the expression of internal stress

$$\sigma_1 = -\frac{\alpha_1 + \alpha_2 \nu}{1-\nu^2} E \Delta T, \tag{13}$$

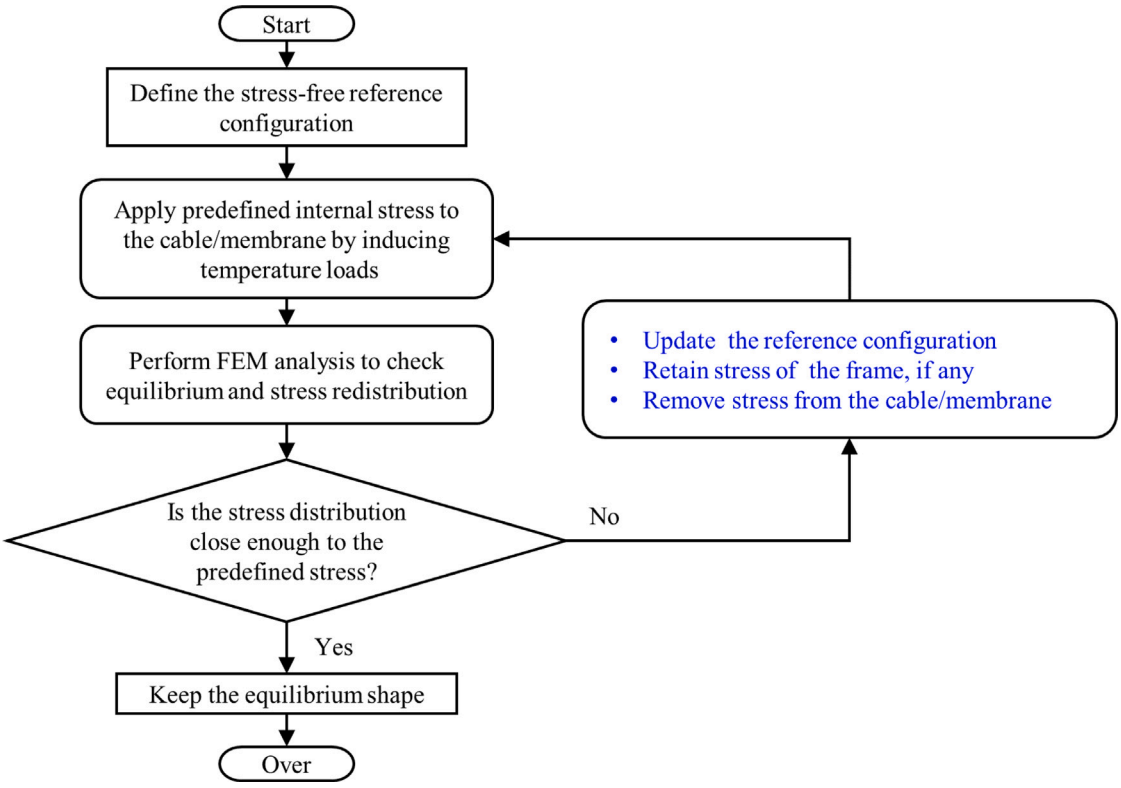


**Fig. 4.** Flowchart of the nonlinear FEM method for form finding.

and

$$\sigma_2 = -\frac{\alpha_1 \nu + \alpha_2}{1-\nu^2} E\Delta T. \tag{14}$$

In a specific scenario where an isotropic stress is desired, i.e., $\sigma_1 = \sigma_2 = \sigma$, and $\alpha_1 = \alpha_2 = \alpha$, the expression for the stress is given by

$$\sigma = -\frac{E\alpha\Delta T}{1-\nu} \tag{15}$$

Therefore, by using Eqs. (13)–(15), any isotropic or orthotropic desired pretension stress state can be generated by carefully choosing the temperature change load and CTEs of the membrane material. Finally, it is essential to highlight that the temperature load, in this context, is a virtual process with no actual physical thermal consequences; instead, it serves as a method to impose pretension in tensile structures effectively [30].

#### 2.2.3. Frame

The frame serves as a supporting structure for the cable and membrane. Depending on the specific modeling requirements, ABAQUS provides the flexibility to represent the frame using various structural elements such as beams, shells, or continuum elements. This adaptability allows for the selection of a suitable element type based on the desired level of detail and accuracy in the structural analysis. The frame can be treated either as a rigid or deformable body by enabling or disabling the *Rigid Body constraint. Finite element nodes are shared among the cable, membrane, and frame at the connecting boundaries, and their connections are defined using the *Tie constraint.

#### 2.2.4. Form finding strategy

The form-finding strategy has been integrated into ABAQUS/Standard, utilizing nonlinear FEM to calculate static equilibrium in each iteration. The analysis steps are as follows, with a flowchart provided in Fig. 4:

**(1) Initial Setup:** Create the initial configuration and establish the finite element model, including the cable, membrane, and frame. This initial configuration serves as the reference state with no initial stress.

**(2) Application of Internal Stress to Cable and Membrane:** Apply predefined internal stress to the cable and membrane. This is achieved by assigning thermal expansion coefficients to the cable and membrane and applying a virtual temperature change as the load.

**(3) Nonlinear Static Analysis:** Perform a nonlinear static analysis to obtain the deformed equilibrium configuration and calculate the stress redistribution in the cable and membrane. This analysis is conducted using the nonlinear static general solver in ABAQUS/Standard. After the simulation, stress redistribution occurs in the cable and membrane, and the rib deforms if it is assumed to be flexible.

**(4) Stress Distribution Check and Iteration:** Verify if the stress distribution closely matches the predefined internal stress. If it does, stop the iteration and retain the equilibrium shape as the final form. If not, initiate the iteration process by updating the configuration and reapplying internal stress to the cable and membrane. Fig. 5 presents a pseudocode for the model update process in ABAQUS. The coordinates of all finite element nodes in the cable, membrane, and frame are recorded and used to update the new configuration using the ABAQUS script "editNode" to modify the mesh node coordinates. The stresses in the cable and membrane are removed from the deformed configuration. For the flexible frame, the deformed shape is updated, and the stress is preserved using the "*Initial State" keyword. In contrast, for the rigid frame, the stress distribution is not applied, and the frame shape is retained. Once the configuration is updated, return to Step (2).

Repeat steps (2), (3), and (4) iteratively until the stresses in the cable and membrane closely match the predefined internal stresses, and there are minimal differences between the shapes of the structure before and after deformation.

## 3. Numerical examples

This section provides verification and validation for the proposed form finding method through several numerical examples. Two benchmark cases are considered, including form finding analyses of a two-dimensional planar membrane with boundary cables and a three-dimensional truncated conic surface. Then, the form finding analysis

```
+-------------------------------------------------------------+
|          Pseudocode of Iteration Process (i = 1 to n)       |
+-------------------------------------------------------------+
| 1. Create a new model by copying the previous one.          |
| 2. Open the ODB file from the previous iteration.           |
| 3. Update coordinates for components:                       |
|    +-----------------------------------------------------+  |
|    | For each component in ['membrane', 'cable', 'frame']: |  |
|    | - Get nodes and their coordinates from ODB file.    |  |
|    | - Apply new coordinates to the current model.       |  |
|    +-----------------------------------------------------+  |
| 4. Set initial state to include stress in the flexible frame. |
| 5. Define contact interactions among components.            |
| 6. Regenerate the model assembly.                           |
| 7. Close the ODB file.                                      |
| 8. Prepare and submit the job.                              |
+-------------------------------------------------------------+
```

**Fig. 5.** Pseudocode of iteration process for form finding in ABAQUS.

of a tent is presented to demonstrate distinctions between rigid frames and flexible frames.

### 3.1. Form finding of cable-membrane structures without frames

First, two well-known shape finding cases are used to benchmark the proposed method. The first example involves the form finding of a planar square-shaped membrane reinforced with four boundary cables. This example was previously analyzed by Tang et al. [24] and Gu et al. [25] through an extended force density method. As illustrated in Fig. 6(a), this example consists of a 100 mm × 100 mm square-shaped membrane with four boundary cables adherent to the edges of the membrane. The four corner points of the membrane are fully constrained. The cables are discretized by linear truss elements (element type T3D2 in ABAQUS) with a circular cross-section of 1.0 mm diameter, and the membrane is modeled with four-node quadrilateral membrane elements (element type M3D4R in ABAQUS) with a thickness of 26.5 μm. The cables are subjected to a pretension force of 50 N, while an isotropic pretension stress of $\sigma_1 = \sigma_2 = 1$ MPa is assumed in the membrane. Both the cable and membrane are treated as linear elastic and isotropic materials, and their respective material properties are summarized in Table 1. Then the form finding was performed using the proposed strategy. Fig. 6(b) displays the final configuration achieved through the form finding process, which matches well with the result predicted by the extended force density method reported in [25]. Stress values at each element node in the membrane were extracted during the iterations, and their root mean square error (RMSE) was defined to quantify the uniformity of the stress distribution. Fig. 6(c) shows the convergence process of RMSE of the Cauthy stress in the 1-direction, with the expression defined as follows.

$$RMSE_{\sigma_{11}} = \sqrt{\frac{\sum_{i=1}^{n}(\hat{\sigma_{11}} - \sigma_{11})^2}{n}} \tag{16}$$

where $\hat{\sigma_{11}}$ represents the predefined value of the internal stress in 1-direction, $\sigma_{11}$ denotes the FEM calculated Cauthy stress value at each element node in the membrane at the equilibrium state of each iteration, and $n$ is the number of nodes in the membrane. It can be seen from Fig. 6(c) that the $RMSE_{\sigma_{11}}$ gradually approaches approximately zero with increasing iterations, indicating the convergence of the stress distribution in the membrane to a uniform state of the prescribed 1 MPa, as also evidenced by the inserted FE snapshots. It is noteworthy that the stresses in the 1-direction and 2-direction are identical in this example because of the symmetric geometry and the isotropic internal stress assumption. Additionally, the pretension force in the cable was extracted to evaluate its convergence. The RMSE of the pretension force in the cable is defined similarly as follows:

**Table 1**
Material properties of the cable and membrane for Example #1.

| | Cable | Membrane |
|---|---|---|
| Young's modulus | $E_c = 20$ GPa | $E_m = 2.17$ GPa |
| Poisson ratio | $\nu_c = 0.3$ | $\nu_m = 0.34$ |
| Coefficient of thermal expansion | $\alpha_c = -2.0\text{e}{-06}/°\text{C}$ | $\alpha_m = 29\text{e}{-6}/°\text{C}$ |

$$RMSE_F = \sqrt{\frac{\sum_{i=1}^{n}(\hat{F} - F)^2}{n}}, \tag{17}$$

where $\hat{F}$ represents the predefined tension force in the cable, $F$ is the tension force at each element node of the cable extracted from the FEM results, and $n$ is the number of nodes in the cable. Fig. 6(d) illustrates the convergence of the RMSE of the pretension force in the cable, showing that as the iterations progress, the $RMSE_F$ gradually approaches zero, and the tension force in the cable stabilizes at a predefined uniform value of 50 N. Finally, we note that in our tests, the 300 iterations required for convergence, as shown in Fig. 6, take approximately 1 h to complete on a PC equipped with an Intel(R) Xeon(R) Silver 4216 CPU @ 2.10 GHz. Although the convergence speed of the proposed nonlinear FEM method is slower than that of the FDM [24,25], the method is developed within commercially available FEM software, making it more user-friendly and easily accessible. With all the scripts made publicly available, we expect our work to facilitate interaction between academia and industry.

The next example consists of the form finding of a three-dimensional truncated conic surface [41]. As shown in Fig. 7(a), the membrane is stretched on two coaxial rigid rings with radius $a = 8$ m and $b = 40$ m respectively, forming a truncated conic surface with a thickness of $t = 1$ mm and a height of $h = 18.3395$ m. The membrane is assumed as a linear elastic and isotropic material, characterized by a Young's modulus of 0.25 GPa, and a Poisson's ratio of 0.34. In theory, when a uniform prestress, i.e., 2.5 MPa, is applied to the membrane, the formed surface will be a minimum surface [42], with analytical expression is

$$Z = -a\left[\ln(\sqrt{X^2 + Y^2} + \sqrt{X^2 + Y^2 - a^2}) - \ln a\right] + h \tag{18}$$

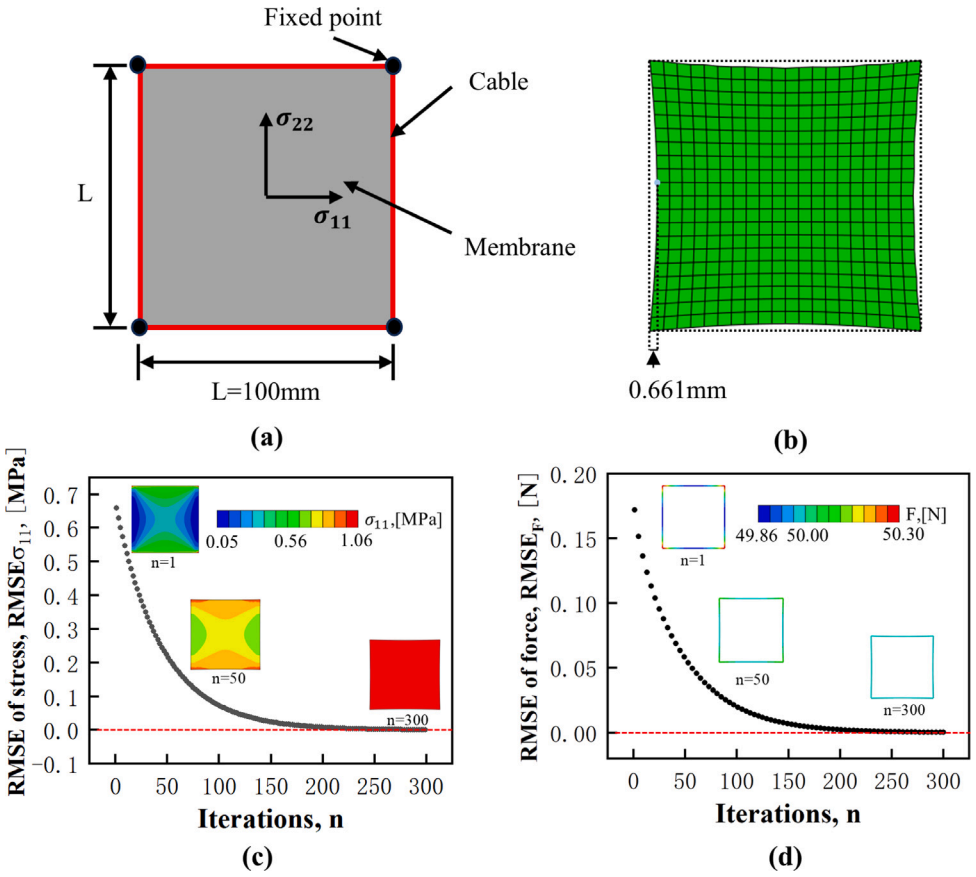


**Fig. 6.** Form finding of a planar cable-membrane structure. (a) Initial configuration showing geometry and boundary conditions. (b) Final configuration obtained from form finding at the iteration of $n = 300$. (c) Iteration process of the internal stress in the membrane. (d) Iteration process of the pretension force in the cable.

and

$$h = a\left[\ln(b + \sqrt{b^2 - a^2}) - \ln a\right] \tag{19}$$

Fig. 7(b) shows that the numerical form finding results are in excellent agreement with the analytical results. Figs. 7(c) and 7(d) give the iteration process of the radial and hoop stress, respectively. As the iteration progresses, the $RMSE_{\sigma_{11}}$ and $RMSE_{\sigma_{22}}$ both converge to approximately zero, and the final stress distribution precisely matches the required prestress state.

### 3.2. Form finding of cable-membrane structure supported with frames

With the accuracy of the proposed method validated, this section moves on to simulating the form finding of a tent-like cable-membrane structure supported with frames. This example illustrates the difference between rigid-frame and flexible-frame boundary conditions in determining the optimal equilibrium shape of the cable-membrane structures. We note that Tang and Li [24] previously examined a similar example using an equivalent force density method; however, in their study, the effect of frames' rigidity was not discussed. Fig. 8(a) shows the initial geometry of the tent. It consists of a hexagonal pyramid with a height $h$ of 1 m, and a base side length $b$ of 1 m. Fig. 8(b) depicts the finite element mesh of the tent-like cable-membrane structure. The base sides are represented by boundary cables, the lateral edges are supporting ribs that serve as frames, and the triangular lateral faces are characterized by membranes. The material and geometric parameters of the cable, membrane, and frame are given in Table 2. We would like to clarify that the material properties listed in Table 2 are sourced from Refs. [14,43]. Specifically, the cable material is Kevlar Aramid Rope, the frame material is SUS 301 steel, and the membrane is a metallic mesh net fabric. For numerical representation, the cable and membrane are discretized by truss and membrane elements, respectively. The frame is discretized by shell elements (element type S4R in ABAQUS). All vertices of the pyramid were fully constrained. A pretension force of 50 N was applied to each boundary cable, and an isotropic prestress of 0.1 MPa was applied to each membrane. Following this, the form finding analysis was conducted. In this example, two cases were simulated for making a comparison, one with the rib treated as a rigid frame and the other with the rib considered as a flexible frame.

Fig. 9(a) presents the iteration process of the RMSE of membrane stress, with $\sigma_{11}$ and $\sigma_{22}$ indicating the radial and hoop stresses, respectively. The results show that the membrane stress stabilizes at a uniform state of 0.1 MPa as $RMSE_\sigma$ approaches 0. Fig. 9(b) displays the RMSE of cable force, indicating that the cable force converges to a uniform value of 50 N, with $RMSE_F$ approaching 0. The inclusion of frame deformations in the iterative form finding process slows down the convergence speed for the flexible frame-supported tent compared to the rigid frame-supported one. Fig. 10 provides a comparison of membrane stress redistribution during form-finding iterations between the tent supported by rigid frames and the one supported by flexible frames. After sufficient iterations, both tents achieve nearly uniform membrane stress distribution. Fig. 11 shows the deformation of flexible frames at the final equilibrium form, along with corresponding coordinate details. It is shown that the flexible frame undergoes a deflection of approximately 2.02% at the midpoint. We acknowledge that the equilibrium form of cable-membrane structures and the deformation of flexible frames are highly dependent on the prestress applied to the cable and membrane, as well as the elastic modulus of the frame. Further elaboration on this aspect will be provided in the subsequent section.

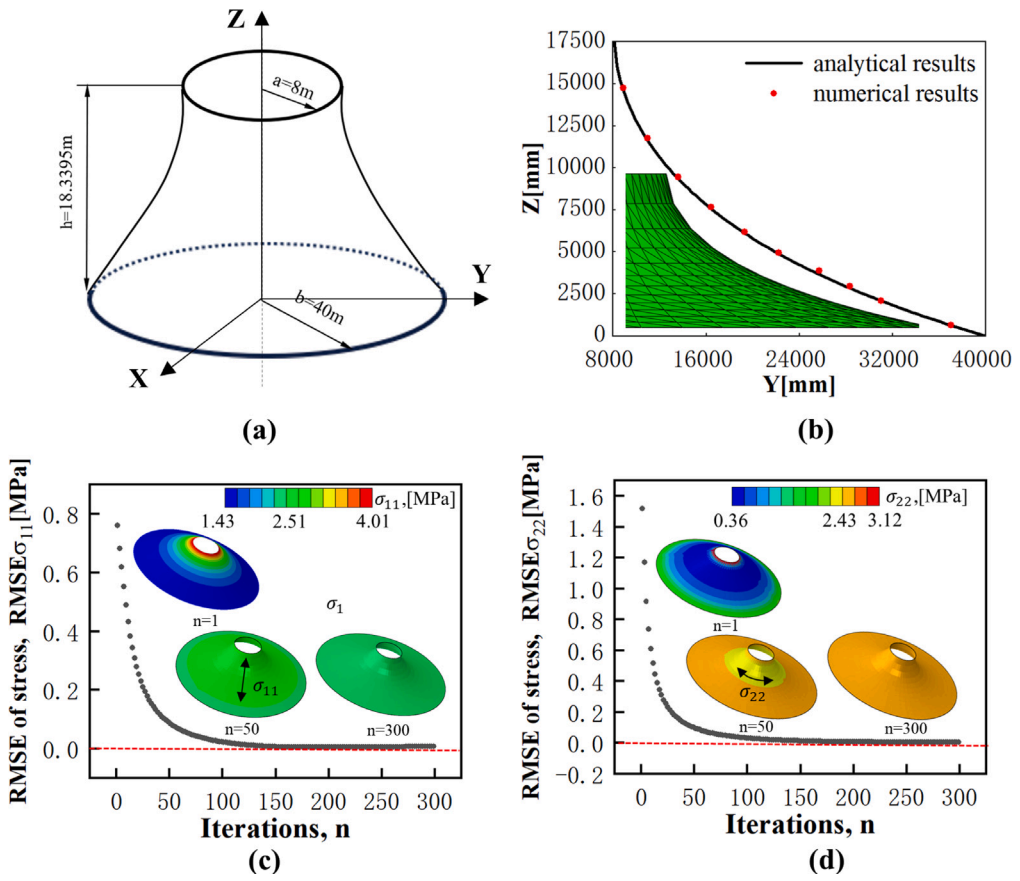


**Fig. 7.** Form finding of a truncated conic surface. (a) Schematic with dimensions. (b) Comparison of analytical and numerical form finding results. Iteration process of the internal stress along the (c) radial and (d) hoop directions.

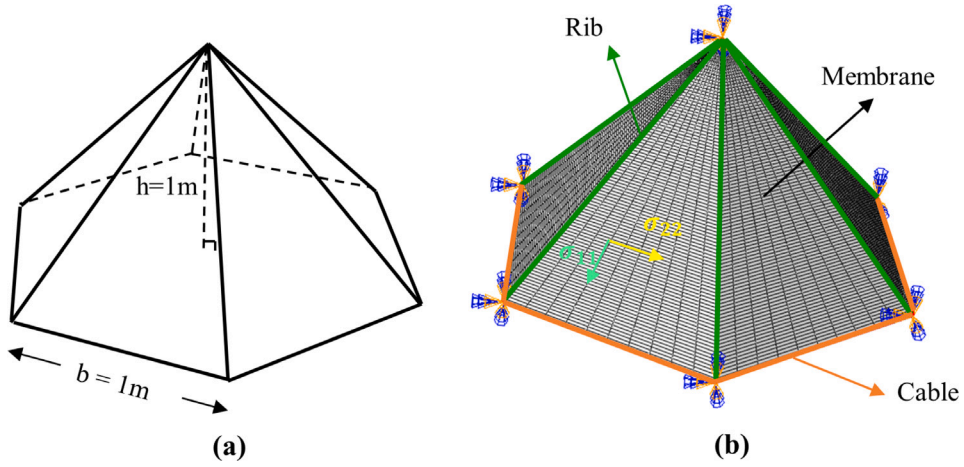


**Fig. 8.** Schematics of the tent-like cable-membrane structure supported with frames. (a) Initial geometry and dimensions. (b) Finite element mesh representation with boundary conditions.

**Table 2**
Material properties for the cable, membrane, and frame.

| | Cable | Membrane | Frame |
|---|---|---|---|
| Young's modulus | $E_c$ = 40 GPa | $E_m$ = 1.7 MPa | $E_f$ = 206 GPa |
| Poisson's ratio | $\nu_c$ = 0.35 | $\nu_m$ = 0.3 | $\nu_f$ = 0.3 |
| CTE | $\alpha_c$ = −3.0e−06/°C | $\alpha_m$ = 1e−5/°C | – |
| Cross-section shape | Circular, 1 mm$^2$ | – | Rectangular, 10 mm × 2 mm |
| Thickness | – | 0.08 mm | – |

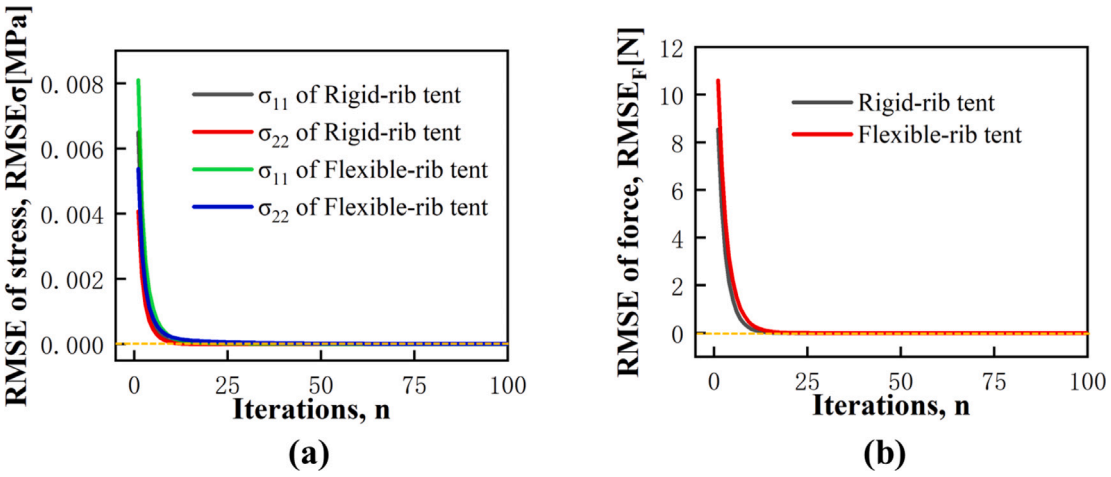


**Fig. 9.** Iteration process of the RMSE of (a) membrane stress and (b) cable force in the tent-like structures.

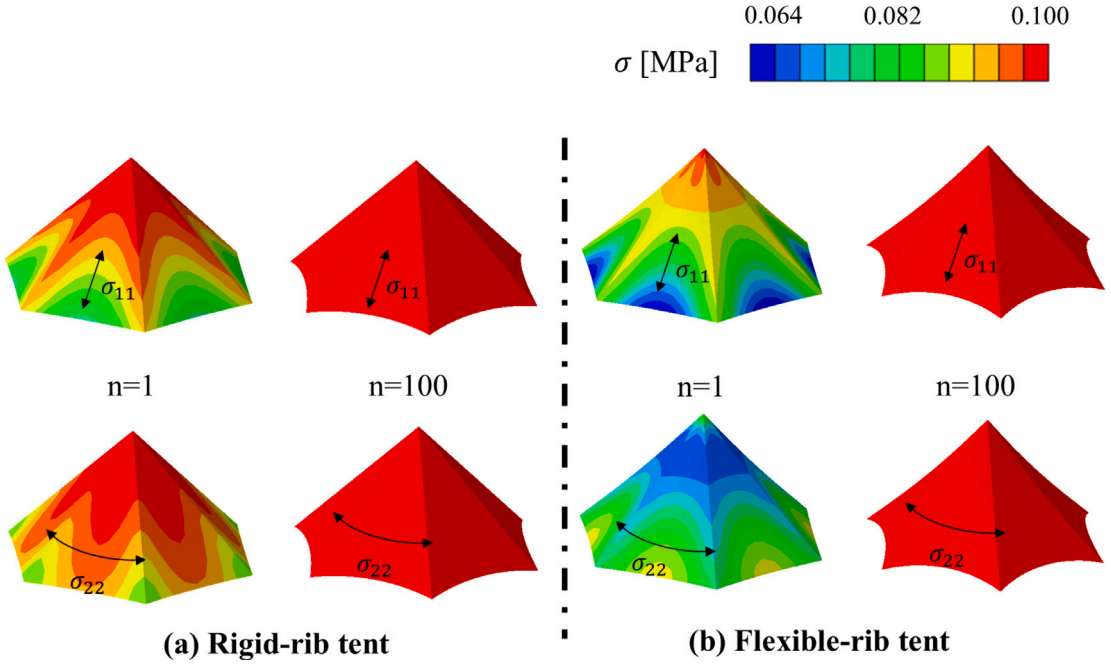


**Fig. 10.** Form-finding results of the tent-like cable-membrane structure under (a) rigid frame support and (b) flexible frame support.

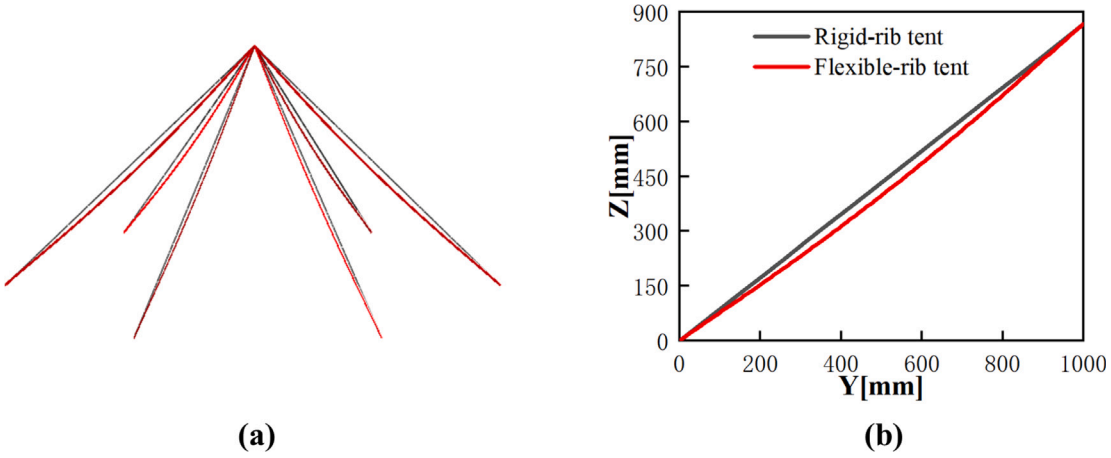


**Fig. 11.** (a) Comparison of the final deformed frames (in red) at the optimal equilibrium form against the initial shape (in black), and (b) the corresponding coordinate details.

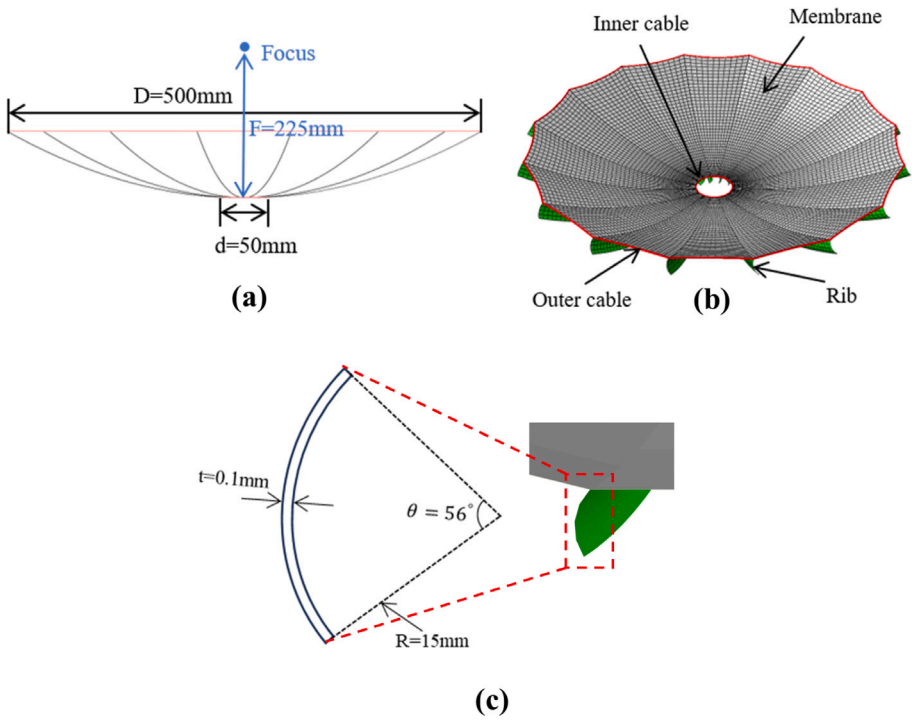


**Fig. 12.** Configuration of the umbrella-like rib-mesh reflector antenna. (a) Schematic illustrating the antenna dimensions. (b) Finite element mesh representation of the antenna. (c) Cross-sectional geometry of the antenna rib.

## 4. Surface accuracy analysis of umbrella rib-mesh reflectors

Having validated the accuracy and efficiency of the proposed form finding method, this section proceeds to its application for performing surface accuracy analysis of the umbrella-like rib-mesh antenna. Emphasis is placed on highlighting the effect of key structural design parameters such as the number and rigidity of the rib, the amount of tension force in the boundary cables, as well as the magnitude and anisotropy of the membrane stress on the surface accuracy of the antenna.

### 4.1. Design of the antenna

Fig. 12(a) shows the geometric configuration of the umbrella-like rib-mesh reflector antenna considered in this study. It features a parabolic membrane surface defined by a focus length $F$ of 225 mm, an aperture diameter $D$ of 500 mm, and an inner diameter $d$ of 50 mm. The membrane is supported by several parabolic ribs at its bottom and is tied to the boundary cables at its inner and outer edges. Fig. 12(b) illustrates the finite element mesh representation of the antenna, including membranes, supporting ribs, and boundary cables. Each radial rib possesses a C-shaped cross-section, as shown in Fig. 12(c), sweeping along the parabolic curve on the top edge. The material properties of the cable, membrane, and rib are the same as given in Table 2. These parameters are adopted from Wu et al. [14,44], where the authors fabricated a 0.5-meter wrapped-rib mesh reflector antenna for deployment testing and surface accuracy characterization. The antenna utilized a stainless steel wire mesh for its reflector surface, stainless steel for its ribs, and Kevlar fiber for its boundary cables.

### 4.2. Effect of number and rigidity of ribs

In this section, we start by investigating the effect of the number and rigidity of ribs on the antenna's surface accuracy by considering multiple simulation cases. In these simulations, an isotropic membrane stress of 0.1 MPa was assumed, and the pretension force for the inner and outer boundary cables was set to 0.1 N and 1.0 N, respectively. The rib number varied from 8, 16, to 24 for comparison, with both rigid and flexible rib assumptions considered. Fig. 13 demonstrates the form finding results of the umbrella-like antenna. The results reveal that the membrane stress distribution tends to become more uniform as the number of ribs increases for both the rigid-rib and flexible-rib antennas. Fig. 13(b) also illustrates the von Mises stress distribution of the flexible ribs in the final equilibrium form. It is noticeable that as the number of ribs increases, the maximum von Mises stress in the rib materials decreases. Moreover, the maximum von Mises stress is measured at 152.3 MPa for $n_{rib} = 8$, significantly below the yield strength of the rib material, which consists of SUS301 SEH stainless steel with a yield strength of 700 MPa [43].

Next, the surface accuracy of the antenna is quantified by the following equation, which assesses how closely the form-finding surface approximates the ideal parabolic shape [45].

$$RMSE = \sqrt{\frac{\sum_{i=1}^{n} A_i(\hat{z}_i - z_i)^2}{\sum_{i=1}^{n} A_i}} \tag{20}$$

where $A_i$ is the projected area of each finite element on the X–Y plane, $\hat{z}_i = \frac{1}{4F}(x_i^2+y_i^2)$ represents the ideal $z$ coordinate of the element centroid calculated using the parabolic equation with the focus length $F$, and $x_i$, $y_i$, and $z_i$ are the coordinates of the element centroid extracted from the form finding procedure, and $n$ denotes the total number of elements on the membrane. The iteration processes of RMSE for the antennas characterized by different numbers and rigidity of ribs are compared in Fig. 14, and the RMSE values at the final equilibrium form are summarized in Table 3. It is shown that the RMSE for all cases converges to a stable level after 100 iterations. However, the RMSE value significantly depends on the number and rigidity of the ribs. As the number of ribs increases, the RMSE becomes smaller, indicating a better surface accuracy of the antenna. Additionally, the flexible-rib antenna exhibits a larger RMSE, indicating worse surface accuracy compared to the rigid-rib antenna. This can be attributed to the deformation of the flexible ribs under the pretension stress and forces in the membrane and cables.

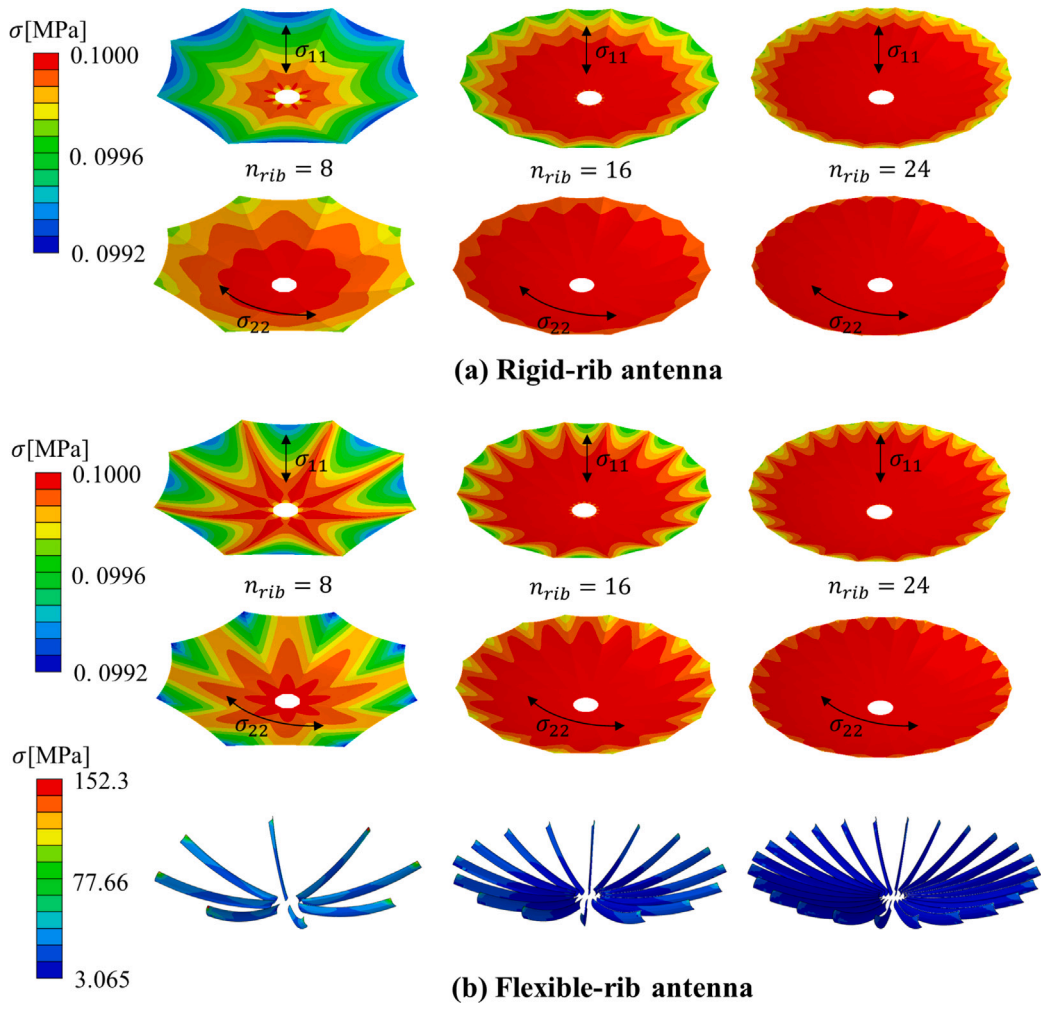


**Fig. 13.** Effect of the number and rigidity of ribs on the form finding results of the umbrella-like rib-mesh antenna. (a) Rigid-rib antenna. (b) Flexible-rib antenna. The respective numbers of ribs are 8, 16, and 24, from the left to the right. The FE snapshots show the membrane stress distribution after 100 form finding iterations. Deformation snapshots of the flexible ribs are also provided, along with the von Mises stress distribution.

**Table 3**
Effect of the number and rigidity of ribs on the surface accuracy error RMSE of the antenna.

| | RMSE [mm] | |
|---|---|---|
| Number of ribs | Rigid rib | Flexible rib |
| 8 | 5.59 | 6.31 |
| 16 | 1.66 | 2.21 |
| 24 | 0.78 | 1.24 |

### 4.3. Effect of pretension stress magnitude in membrane and cable

Next, the investigation considers the effect of the magnitude of prestress in the membrane and pretension forces in the boundary cables. In these cases, the number of ribs is fixed at 16, and the flexible rib assumption is utilized. Three sets of membrane stress, $\sigma_M = 0.1, 0.15$, and 0.2 MPa, along with three sets of pretension forces in cables, $T_{IN} = 0.1$ N & $T_{OUT} = 1.0$ N, $T_{IN} = 0.1$ N & $T_{OUT} = 0.1$ N, $T_{IN} = 1.0$ N & $T_{OUT} = 1.0$ N, result in a total of nine simulation cases. The iteration processes of surface accuracy error RMSE of these antenna cases are shown in Fig. 15. The stress distributions in the membrane at the final equilibrium form obtained through form-finding are shown in Figs. 16 and 17, with the surface accuracy error RMSE values summarized in Table 4. It can be observed from the results of each column that as the membrane stress increases, the surface accuracy error RMSE slightly increases, indicating a worse surface accuracy. This is because a larger membrane stress causes more significant deformation of the radial ribs. By comparing the results within each row, it can be observed that the RMSE of the antenna for the case $T_{IN} = 0.1$ N and $T_{OUT} = 1.0$ N is almost the same as that of the case $T_{IN} = 1.0$ N and $T_{OUT} = 1.0$ N. This suggests that the pretension force in the inner cables has a limited effect on the surface accuracy and stress distribution of the antenna. Furthermore, by comparing the results for the case $T_{IN} = 0.1$ N and $T_{OUT} = 1.0$ N to the case $T_{IN} = 0.1$ N and $T_{OUT} = 0.1$ N, it becomes evident that the pretension force in the outer cables significantly impacts the surface accuracy and stress distribution of the antenna. A smaller pretension force in the outer cables leads to a smaller RMSE but a larger $\text{RMSE}_\sigma$, indicating that a smaller pretension force in the outer cables results in slightly better surface accuracy but worse stress distribution uniformity. Fig. 18 presents deformation snapshots of the flexible ribs at the final equilibrium form along with the von Mises stress distribution. It illustrates that higher membrane prestress results in increased stress distribution in the ribs, yet the maximum von Mises stress remains well below the material's yield strength.

### 4.4. Effect of membrane stress anisotropy

In this section, we explore the effect of membrane stress anisotropy on the antenna's surface accuracy. It should be noted that the mesh

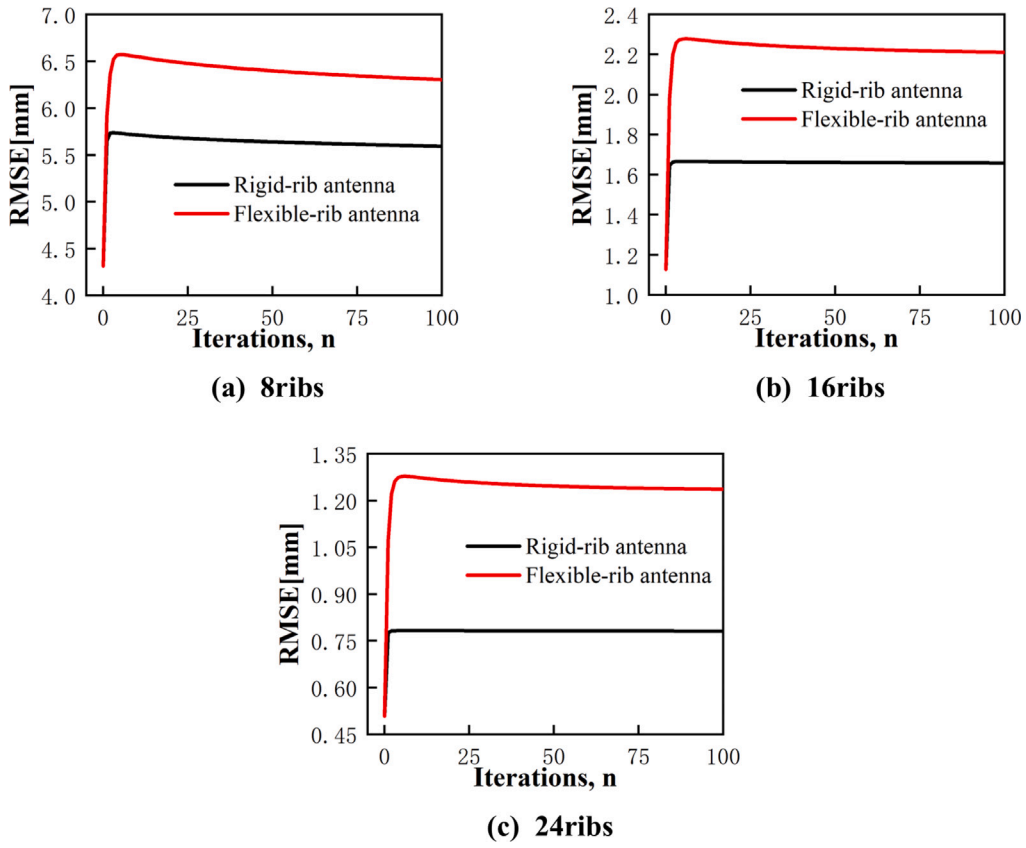


**Fig. 14.** Effect of the number and rigidity of ribs on the iteration process of the surface accuracy error RMSE of the antenna.

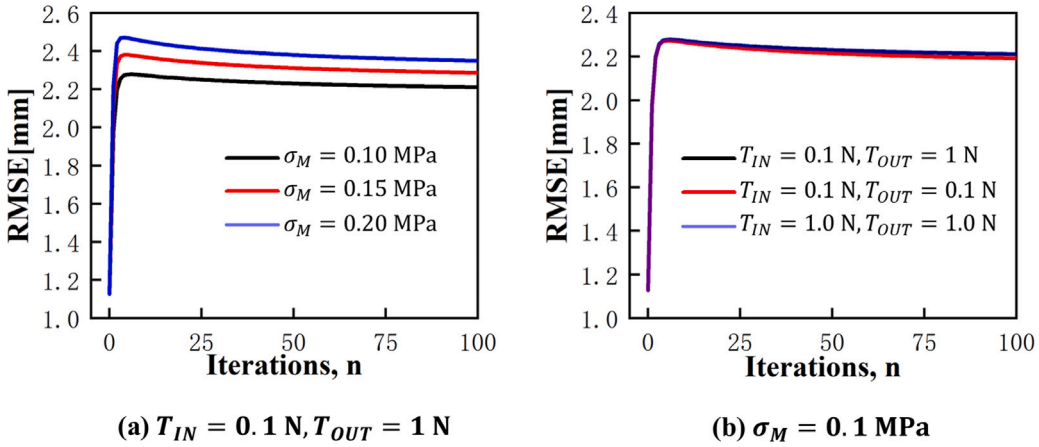


**Fig. 15.** Effect of the (a) tension force in the inner and outer cables and the (b) membrane stress on the surface accuracy error RMSE of the antenna.

**Table 4**
Effect of boundary cable tension and membrane stress on the surface accuracy error RMSE of the antenna.

| | RMSE [mm] | | |
|---|---|---|---|
| | $T_{IN}$ = 0.1N $T_{OUT}$ = 1.0N | $T_{IN}$ = 0.1N $T_{OUT}$ = 0.1N | $T_{IN}$ = 1.0N $T_{OUT}$ = 1.0N |
| $\sigma_m$ = 0.10 MPa | 2.21 | 2.19 | 2.21 |
| $\sigma_m$ = 0.15 MPa | 2.29 | 2.27 | 2.29 |
| $\sigma_m$ = 0.20 MPa | 2.35 | 2.34 | 2.35 |

membrane comprises metal wires arranged in specific weaving patterns. The mechanical behavior of the membrane depends on various factors including the metal properties, weave pattern, wire diameter, and surface treatment, which can be usually anisotropic. The anisotropy level of the mesh can vary depending on the weave patterns, e.g., plain-wave fabric typically exhibits significant isotropy, while weft-knitted and wrap-knitted fabrics can demonstrate substantial anisotropy [7,46–48]. Specifically, Li et al. [7] analyzed the orthotopic elastic properties of a two-bar tricot mesh reflector with the method of fractal mechanics analysis of wire meshes. Zhang et al. [48] characterized the anisotropic elastic modulus of wrap-knitted wire mesh through a combination of biaxial tensile simulation and experiment. They utilized the nonlinear FEM method to explore the influence of the wire mesh's anisotropic properties on the form-finding design results of an AstroMesh antenna. In this section, although the membrane is assumed isotropic in modulus, we can introduce an anisotropic membrane stress into the model for exploration. We consider five antenna configurations with 16 flexible

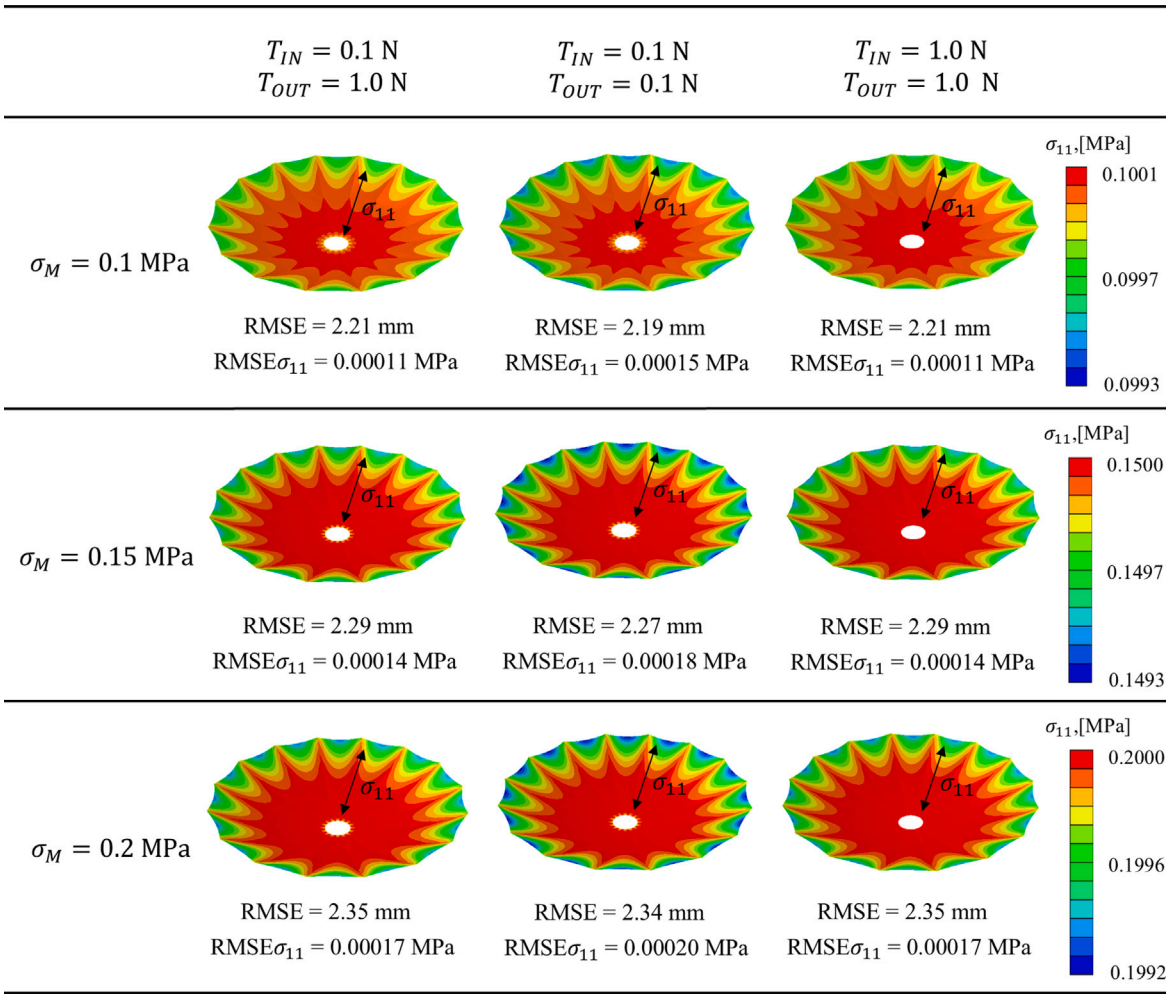


**Fig. 16.** Effect of the tension force in the inner and outer cables and the internal stress in the membrane on the form finding results of the umbrella-like rib-mesh antenna. The FE snapshots show the distribution of membrane stress at the optimal equilibrium form along the radial direction.

ribs, where the pretension forces in the boundary cables are set to $T_{IN}$ = 0.1 N and $T_{OUT}$ = 1.0 N. To introduce anisotropy in the membrane, different membrane stress values are applied in the radial and circumferential directions. Fig. 19 and Table 5 illustrate the significant impact of membrane stress anisotropy on the surface accuracy error RMSE of the antenna. In cases with identical radial stress, a higher stress in the circumferential direction correlates with a reduced RMSE, implying improved surface accuracy. Conversely, among cases with consistent circumferential stress, a greater radial stress corresponds to a higher RMSE, indicating poorer surface accuracy. Therefore, a larger circumferential stress is preferred to obtain a better surface accuracy of the antenna. This finding also corroborates the results reported by Wu et al. [14]. Finally, the form finding results for these cases are depicted in Fig. 20. It is evident that the radial membrane stress has a more pronounced effect on the deformation of the flexible ribs compared to the circumferential direction. This is indicated by the larger maximum von Mises stress in the rib materials induced by the radial stress. We also note that the largest von Mises stress observed is still well below the yield strength of the rib material.

**Table 5**
Effect of membrane stress anisotropy on the surface accuracy error RMSE of the antenna.

| Membrane pretension [MPa] | | RMSE [mm] |
|---|---|---|
| Radial tension, $\sigma_{11}$ | Circumferential tension, $\sigma_{22}$ | |
| 0.10 | 0.20 | 2.05 |
| 0.10 | 0.15 | 2.09 |
| 0.10 | 0.10 | 2.21 |
| 0.15 | 0.10 | 2.43 |
| 0.20 | 0.10 | 2.64 |

## 5. Concluding remarks

Deployable rib-mesh reflector antennas have been extensively utilized for communication purposes in various space missions. This type of spaceborne antenna typically comprises a mesh surface supported by ribs and cables, forming a tensile cable-membrane structure supported with frames. Surface accuracy, which assesses how closely the deployed mesh surface approximates the ideal parabolic shape, is a critical factor that determines the electrical performance of the antenna. The surface accuracy of the rib-mesh reflector antenna could be dependent on the membrane stress state, the pretension force within the boundary cables, as well as the deformation of the supporting ribs. Form finding is an essential method for determining the optimal equilibrium shape and the surface accuracy of the mesh surface under a prescribed internal stress state. However, most existing form finding studies on rib-mesh reflectors have focused on loop mesh reflector antennas, which rely on the form finding of cable networks. The form finding analysis for umbrella-like parabolic rib-supported mesh reflector surfaces remains largely unexplored.

The paper develops a nonlinear FEM code that addresses the form finding of cable-membrane structures supported by flexible frames. The fundamental mechanics and the implementation details of the

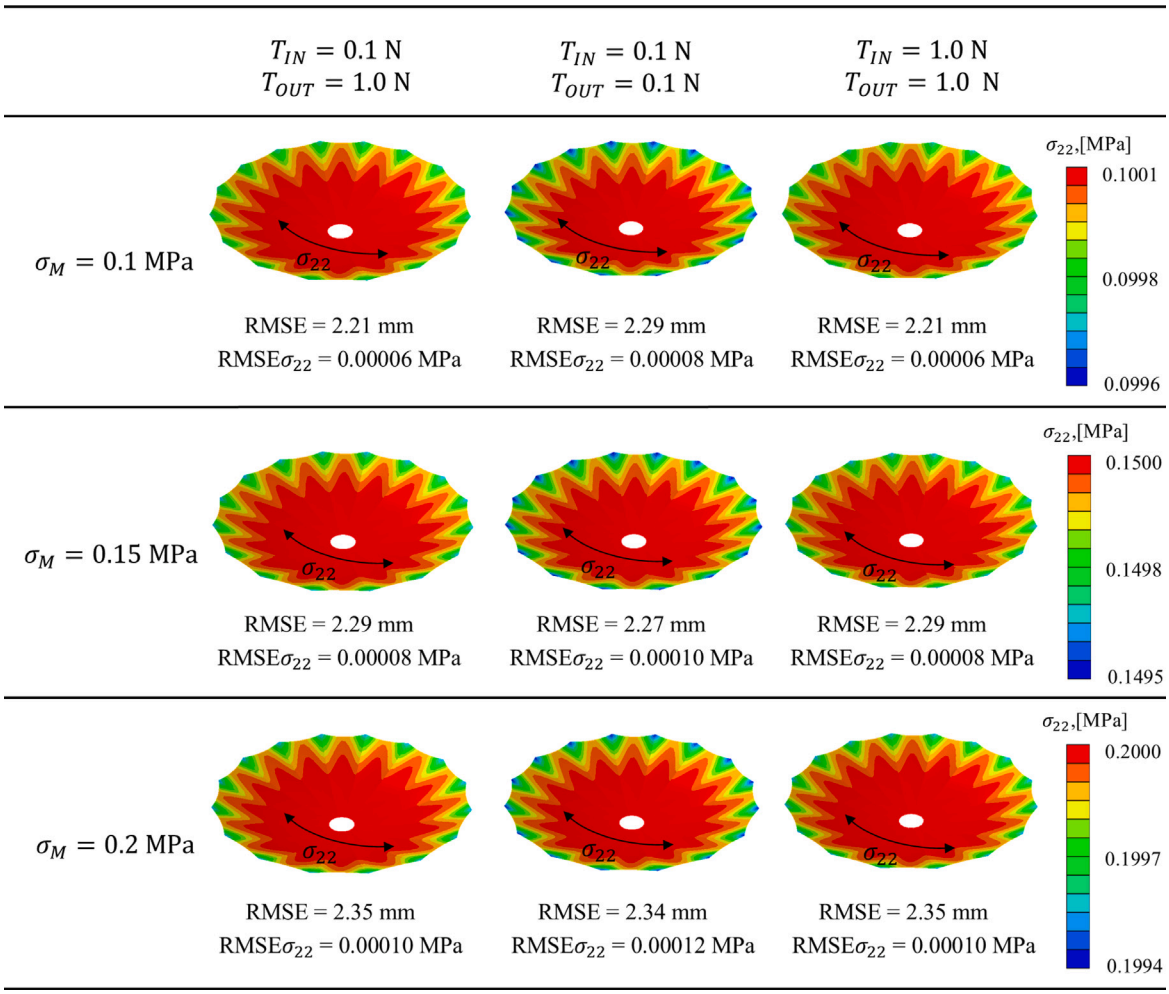


**Fig. 17.** Effect of the tension force in the inner and outer cables and the internal stress in the membrane on the form finding results of the umbrella-like rib-mesh antenna. The FE snapshots show the distribution of membrane stress at the optimal equilibrium form along the hoop direction.

method were documented. Subsequently, form finding analyses of a two-dimensional planar cable-membrane structure and a three-dimensional truncated conic surface were performed, and the results obtained using the proposed method matched well with literature-reported results or analytical results, confirming the accuracy of the proposed method. Following that, a tent-like frame-supported cable-membrane structure was introduced for form finding to highlight differences between rigid frame-supported and flexible frame-supported cable-membrane structures, further validating the efficiency of the method. Finally, the method was applied to conduct surface accuracy analysis of an umbrella-like parabolic rib-supported mesh reflector antenna. Parametric analyses were conducted to investigate the effects of the number and rigidity of ribs, the magnitude and anisotropy of membrane stress, and the pretension forces within boundary cables on the antenna's surface accuracy. The main findings are as follows: (i) Increasing the number of ribs improves surface accuracy, and a rigid-rib antenna outperforms a flexible-rib antenna with identical design parameters. (ii) The pretension force within the inner boundary cables has a negligible effect on stress distribution and surface accuracy, whereas higher pretension force in outer boundary cables improves stress distribution uniformity but slightly reduces surface accuracy. (iii) Greater membrane stress in the circumferential direction results in improved surface accuracy, while greater membrane stress in the radial direction reduces surface accuracy.

The main contributions of this paper are as follows. First, the iterative form-finding method has been successfully integrated into the commercial FEM software, ABAQUS, via the Python scripting interface. This integration automates the iterative equilibrium calculations required for the form-finding process, significantly enhancing overall efficiency. We have provided detailed implementation steps and made the source code for a set of benchmark numerical examples openly accessible, offering a user-friendly and easily customizable tool for scientists and engineers. Additionally, the method has been applied to analyze form-finding and surface accuracy in umbrella-like rib-mesh reflectors. Parametric studies were conducted to highlight the influence of key design parameters-such as the number and rigidity of ribs, the magnitude and anisotropy of membrane stress, and the pretension force in boundary cables-on the antenna's surface accuracy, providing valuable insights for the design of umbrella-like rib-mesh antennas.

Moreover, we note that designing a self-deployable flexible rib umbrella antenna for real-world applications involves meeting several key requirements: the distribution of pretension forces and stresses in the boundary cables and mesh membranes, the surface accuracy of the deployed reflector, and the folding and deployment capability of the system. Our current work primarily addresses the first of these requirements through the form-finding analysis, achieving an equilibrium form that balances the uniform stresses in the cable and mesh with the deformation of the flexible ribs. This uniform stress distribution is crucial for determining the overall stiffness of the system, as the stiffness of the mesh and cable is directly influenced by the tension stress [49]. However, the equilibrium form may present challenges related to surface accuracy due to rib deformation, as well as issues with the folding and deployment behavior of the antenna. Future work

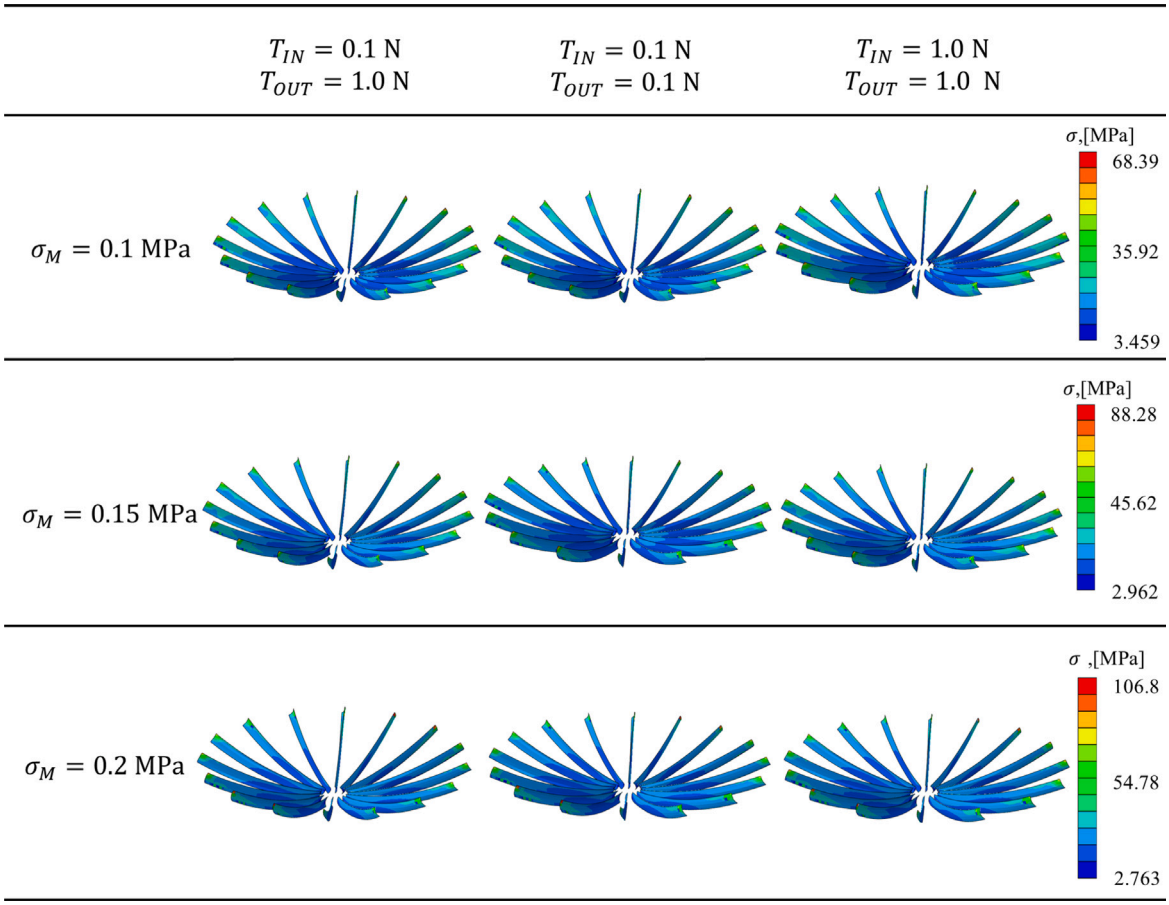


**Fig. 18.** Deformation snapshots depict the von Mises stress distribution of the flexible ribs at the optimal equilibrium form.

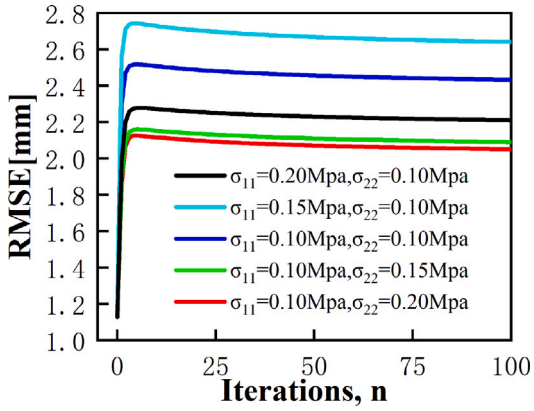


**Fig. 19.** Effect of membrane stress anisotropy on the iteration process of the surface accuracy error RMSE of the antenna.

may focus on designing the geometric design and material parameters of the ribs, mesh, and cables to ensure that the equilibrium state achieved through form-finding meets the required surface accuracy. This can be achieved through an inverse optimization method that would use the surface accuracy of the reflector as the objective and the design parameters of the ribs, mesh, and cables as design variables, as highlighted in studies such as [14]. In addition, another research direction would be to investigate the folding and deployment behavior of the ribs, mesh, and cables. The rib design must allow for compact folding without material failure, ensuring that it can store sufficient strain energy in the stowed state and deploy effectively to open the mesh and cable [10,50]. We believe our work provides a valuable method that can facilitate surface accuracy optimization and contribute to the design of umbrella-like antennas.

Finally, we acknowledge that the choice of initial reference configuration is crucial for ensuring computational convergence and efficiency in form-finding. In this paper, planar membranes are used as the initial configuration to facilitate convergence. However, for more complex cable-membrane structures-such as those with fixed anchor points at different levels or involving non-minimal surfaces-the initial configuration may not be straightforward, potentially leading to convergence issues [34,51]. Such scenarios may require advanced initialization techniques or additional iterative steps to achieve a stable solution. Moreover, we recognize that the proposed FEM-based method holds potential for addressing the form-finding of cable nets in AstroMesh-like reflectors. This would, however, necessitate the development of specific Python scripts, and the method might be less efficient compared to the well-established Force Density Method (FDM). Nonetheless, given the accessibility of commercial FEM software to engineers, it could be worthwhile to explore and compare the accuracy and efficiency of this approach against FDM in future studies.

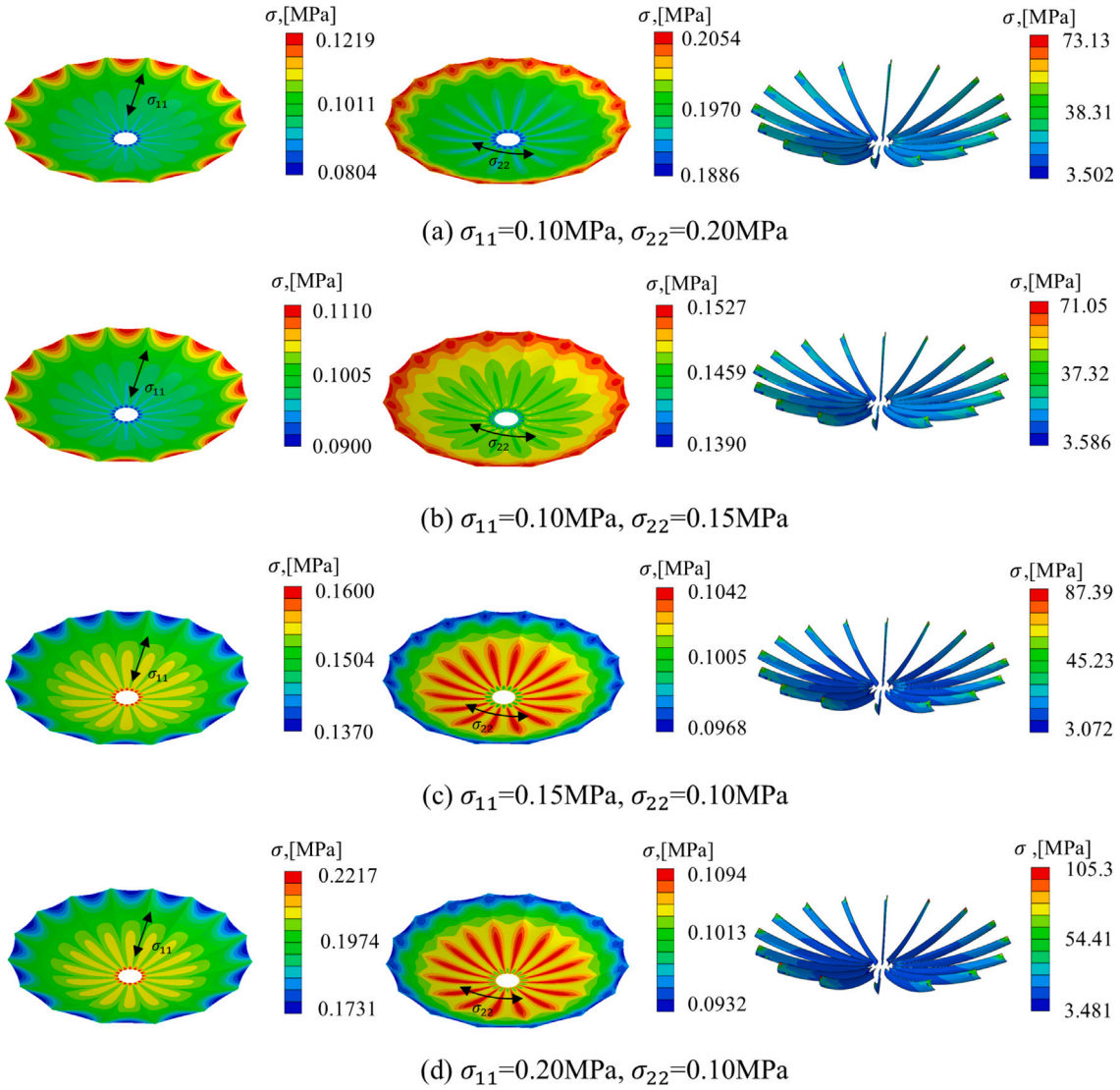


**Fig. 20.** Effect of membrane stress anisotropy on the form finding results of the umbrella-like rib-mesh antenna. The FE snapshots at the left and middle show the distribution of membrane stress at the optimal equilibrium along the radial and hoop directions, respectively. The FE snapshots at the right panel show the von Mises stress distribution of the flexible ribs.

## Data availability

The code required to reproduce these findings is available to download from https://github.com/SCU-An-Group/FEM-based-Form-Finding.

## CRediT authorship contribution statement

**Shiran Zhu:** Investigation, Methodology, Software. **Ruiwen Guo:** Investigation. **Xin Jin:** Conceptualization. **Xiaofei Ma:** Conceptualization, Resources. **Jinxiong Zhou:** Validation. **Ning An:** Conceptualization, Funding acquisition, Investigation, Methodology, Supervision, Validation, Writing – original draft, Writing – review & editing.

## Declaration of competing interest

The authors declare that they have no known competing financial interests or personal relationships that could have appeared to influence the work reported in this paper.

## Acknowledgments

This research was supported by the National Natural Science Foundation of China (No. 12202295), and the Fundamental Research Funds for the Central Universities, People's Republic of China (No. YJ2021137).

## References

[1] Liu C, Deng X, Liu J, Peng T, Yang S, Zheng Z. Dynamic response of saddle membrane structure under hail impact. Eng Struct 2020;214:110597.
[2] Sakamoto H, Park K, Miyazaki Y. Evaluation of membrane structure designs using boundary web cables for uniform tensioning. Acta Astronaut 2007;60(10–11):846–57.
[3] He Y, Zhu M, Zhao Y, Li X. Influence of different cable–membrane connection models on wind-induced responses of an air supported membrane structure with orthogonal cable net. Thin-Walled Struct 2022;180:109840.
[4] Chandra M, Kumar S, Chattopadhyaya S, Chatterjee S, Kumar P. A review on developments of deployable membrane-based reflector antennas. Adv Space Res 2021;68(9):3749–64.
[5] Ma X, Li T, Ma J, Wang Z, Shi C, Zheng S, et al. Recent advances in space-deployable structures in China. Engineering 2022;17:207–19.

[6] Scialino G, Salvini P, Migliorelli M, Pennestrì E, Valentini P, Van't Klooster K, et al. Structural characterization and modeling of metallic mesh material for large deployable reflectors. In: Proceedings of the 2nd international conference on advanced lightweight structures and reflector antennas, tbilisi, Georgia. 2014, p. 182–92.
[7] Li T, Jiang J, Shen T, Wang Z. Analysis of mechanical properties of wire mesh for mesh reflectors by fractal mechanics. Int J Mech Sci 2015;92:90–7.
[8] Chahat N, Sauder J, Hodges R, Thomson M, Samii YR, Peral E. Ka-band high-gain mesh deployable reflector antenna enabling the first radar in a CubeSat: RainCube. In: 2016 10th European conference on antennas and propagation. IEEE; 2016, p. 1–4.
[9] Deng J, An N, Jia Q, Ma X. Deployment analysis of composite thin-walled lenticular tubes with effect of storage time and temperature. Chin J Aeronaut 2024;37(1):162–72.
[10] Guo R, Jin X, Jia Q, Ma X, An N, Zhou J. Folding, stowage, and deployment of composite thin-walled lenticular tubes. Acta Astronaut 2023;213:567–77.
[11] Russell R, Campbell T, Freeland R. A technology development program for large space antennas. Tech. rep., 1980.
[12] Angevain J-C, Ihle A, Rodrigues G, Santiago-Prowald J. Large deployable spaceborne reflector antennas in Europe: progress status and perspectives. In: 2019 13th European conference on antennas and propagation. IEEE; 2019, p. 1–5.
[13] Urata KN, Sumantyo JTS, Santosa CE, Viscor T. A compact C-band CP-SAR microsatellite antenna for earth observation. Acta Astronaut 2019;159:517–26.
[14] Wu D, Wu M, Xiang P, Yan Z. Surface accuracy analysis and optimization design of rib-mesh paraboloidal antenna reflectors. Aerosp Sci Technol 2022;129:107817.
[15] Pellegrino S. Deployable membrane reflectors. In: Proc. 2nd world engineering congress (July 22-25, 2002, sarawak, Malaysia). 2002, p. 1–9.
[16] Lai C, Pellegrino S. Design and testing of a 1.5 m offset CRTS demonstrator. Department of Engineering, University of Cambridge; 2001.
[17] An N, Li M, Zhou J. Modeling SMA-enabled soft deployable structures for kirigami/origami reflectors. Int J Mech Sci 2020;180:105753.
[18] Lim JH, Kim Y-B, Jang I-S, Kim H, Oh H-U. Parabolic deployable mesh antenna with a hingeless system of superelastic SMA ribs and composite tape springs. Acta Astronaut 2022;200:149–62.
[19] Veenendaal D, Block P. An overview and comparison of structural form finding methods for general networks. Int J Solids Struct 2012;49(26):3741–53.
[20] Li T, Zuowei W, Deng H. Mesh reflector antennas: form-finding analysis review. In: 54th AIAA/aSME/ASCE/AHS/aSC structures, structural dynamics, and materials conference. 2013, p. 1576.
[21] Schek H-J. The force density method for form finding and computation of general networks. Comput Methods Appl Mech Engrg 1974;3(1):115–34.
[22] Maurin B, Motro R. The surface stress density method as a form-finding tool for tensile membranes. Eng Struct 1998;20(8):712–9.
[23] Li T, Jiang J, Deng H, Lin Z, Wang Z. Form-finding methods for deployable mesh reflector antennas. Chin J Aeronaut 2013;26(5):1276–82.
[24] Tang Y, Li T. Equivalent-force density method as a shape-finding tool for cable-membrane structures. Eng Struct 2017;151:11–9.
[25] Gu Y, Du J, Yang D, Zhang Y, Zhang S. Form-finding design of electrostatically controlled deployable membrane antenna based on an extended force density method. Acta Astronaut 2018;152:757–67.
[26] Yuan S, Yang B, Fang H. Form-finding of large deployable mesh reflectors with elastic deformations of supporting structures. In: 2018 AIAA spacecraft structures conference. 2018, p. 1198.
[27] Nie R, He B, Hodges DH, Ma X. Form finding and design optimization of cable network structures with flexible frames. Comput Struct 2019;220:81–91.
[28] Liu R, Guo H, Liu R, Tang D, Wang H, Deng Z. Design and form finding of cable net for a large cable–rib tension antenna with flexible deployable structures. Eng Struct 2019;199:109662.
[29] Thomson MW. The AstroMesh deployable reflector. In: IUTAM-IASS symposium on deployable structures: theory and applications: proceedings of the IUTAM symposium held in Cambridge, UK, 6–9 September 1998. Springer; 2000, p. 435–46.
[30] Jones TC, Bart-Smith H, Mikulas M, Watson J. Finite element modeling and analysis of large pretensioned space structures. J Spacecr Rockets 2007;44(1):183–93.
[31] Valdés J, Miquel J, Oñate E. Nonlinear finite element analysis of orthotropic and prestressed membrane structures. Finite Elem Anal Des 2009;45(6–7):395–405.
[32] Shi J-X, Wu Z, Tsukimoto S, Shimoda M. Design optimization of cable–membrane structures for form-finding and stiffness maximization. Compos Struct 2018;192:528–36.
[33] Zhang S, Zhang S, Zhang Y, Ye J. Force density sensitivity form-finding design method for cable-mesh reflector antennas considering interactive effects between cable network and supporting truss. Eng Struct 2021;244:112722.
[34] Marbaniang AL, Dutta S, Ghosh S. Updated weight method: an optimisation-based form-finding method of tensile membrane structures. Struct Multidiscip Optim 2022;65(6):169.
[35] Bletzinger K-U, Ramm E. A general finite element approach to the form finding of tensile structures by the updated reference strategy. Int J Space Struct 1999;14(2):131–45.
[36] Bletzinger K-U, Wüchner R, Daoud F, Camprubí N. Computational methods for form finding and optimization of shells and membranes. Comput Methods Appl Mech Engrg 2005;194(30–33):3438–52.
[37] Liu C, Wang M, Deng X, Li D, Liu J, Wang X. Impact of saddle membrane structure by hail with combined particle sizes: Numerical simulation and experimental investigation. Eng Struct 2022;264:114477.
[38] Li J-J, Chan S-L. An integrated analysis of membrane structures with flexible supporting frames. Finite Elem Anal Des 2004;40(5–6):529–40.
[39] Cai J, Qian R, Lin Q, Pan L, Kueh AB, Zhang Q, et al. Form-finding analysis and optimization of cable membrane structure based on iterative correction of tension process. Adv Space Res 2023;71(6):2745–58.
[40] Yang D, Zhang Y, Li P, Du J. Numerical form-finding method for large mesh reflectors with elastic rim trusses. Acta Astronaut 2018;147:241–50.
[41] Chang-yong S. Analysis of tensioned membrane structures considering cable sliding. J Zhejiang Univ-Sci A 2003;4(6):672–82.
[42] Dierkes U, Hildebrandt S, Küster A, Wohlrab O, Dierkes U, Hildebrandt S, et al. Minimal surfaces. Springer; 1992.
[43] Wu Z, Xiang P, Wu M, Niu C, Guan F. Design, analysis and testing of a 0.5 m diameter wrapped rib-tensioned surface reflector demonstrator. In: Proceedings of IASS annual symposia, vol. 2018, (14):International Association for Shell and Spatial Structures (IASS); 2018, p. 1–5.
[44] Zhang H, Wu M, Xiang P. Surface accuracy analysis and test on 0.5 m aperture wrap-rib deployable antenna. In: Proceedings of IASS annual symposia, vol. 2023, (20):International Association for Shell and Spatial Structures (IASS); 2023, p. 1–12.
[45] Maddio P, Meschini A, Sinatra R, Cammarata A. An optimized form-finding method of an asymmetric large deployable reflector. Eng Struct 2019;181:27–34.
[46] Zhang J, He B, Nie R, Wang G, Zhang L, Yu H, et al. High-accuracy design for mesh antennas considering the metallic mesh. Int J Mech Sci 2022;226:107415.
[47] Shao H, Li J, Chen N, Shao G, Jiang J, Yang Y. Experimental study on bi-axial mechanical properties of warp-knitted meshes with and without initial notches. Materials 2018;11(10):1999.
[48] Zhang Y, Zhang H, Yang D, Qin Q, Zhu R. Form-finding design of cable–mesh deployable reflector antennas considering wire mesh properties. AIAA J 2019;57(11):5027–41.
[49] Kukathasan S, Pellegrino S. Vibration of prestressed membrane reflectors. Citeseer; 2001.
[50] Jin H, Jia Q, An N, Zhao G, Ma X, Zhou J. Surrogate modeling accelerated shape optimization of deployable composite tape-spring hinges. AIAA J 2022;60(10):5942–53.
[51] Kabasi S, Marbaniang AL, Ghosh S. Gradient enhanced physics-informed neural network for iterative form-finding of tensile membrane structures by potential energy minimization. Eur J Mech A Solids 2024;106:105332.